Faster and Healthier Charging of Lithium-Ion Batteries via Constrained Feedback Control

Luis D. Couto¹⁰, Raffaele Romagnoli¹⁰, *Member, IEEE*, Saehong Park¹⁰, Dong Zhang¹⁰, *Member, IEEE*, Scott J. Moura¹⁰, *Member, IEEE*, Michel Kinnaert¹⁰, *Member, IEEE*, and Emanuele Garone¹⁰, *Member, IEEE*

Abstract—A constrained feedback control strategy designed on the basis of a simplified electrochemical-thermal model is considered for the fast and healthy charging of a lithium-ion battery cell. The constraints ensure avoidance of side reactions and operating modes that yield premature aging (healthier charging). They are enforced through a reference governor approach, hence requiring a low computational burden. A systematic approach is presented for model identification and control law design. The method is first validated on a detailed battery simulator based on the Doyle-Fuller-Newman model combined with a thermal model. Next, it is validated experimentally through battery-inthe-loop long-term aging campaigns, and the results show that the charging time is reduced by 22% while simultaneously ensuring a longer lifetime (26% less capacity degradation) compared to a 2C constant-current/constant-voltage (CCCV) approach. Compared to recommended C/2 CCCV, our method charges the battery 70% faster and degrades it similarly despite more demanding operating conditions.

Index Terms—Constrained feedback control, electrochemical model, fast healthy charging, lithium-ion (Li-ion) battery, long-term battery aging, reference governor (RG).

Nomenclature

Electrochemical Parameters:

 c_e Electrolyte concentration (mol·m⁻³). $c_{s,\text{max}}$ Maximum solid concentration (mol·m⁻³).

CSC Critical surface concentration.

Manuscript received May 17, 2021; revised October 6, 2021; accepted November 22, 2021. Manuscript received in final form December 10, 2021. This work was supported in part by the Fonds de la Recherche Scientifique (FNRS) under Grant T.0142.20 and in part by the Formation à la Recherche dans l'Industrie et dans l'Agriculture (FRIA) Grant. The work of Luis D. Couto was supported by the Wiener-Anspach Foundation. Recommended by Associate Editor D. M. Raimondo. (Corresponding author: Luis D. Couto.)

Luis D. Couto, Michel Kinnaert, and Emanuele Garone are with the Department of Control Engineering and System Analysis, Université libre de Bruxelles, B-1050 Brussels, Belgium (e-mail: lcoutome@ulb.ac.be; michel.kinnaert@ulb.ac.be; egarone@ulb.ac.be).

Raffaele Romagnoli is with the Department of Electrical and Computer Engineering, Carnegie Mellon University, Pittsburgh, PA 15213 USA (e-mail: rromagno@andrew.cmu.edu).

Saehong Park and Scott J. Moura are with the Energy, Controls, and Applications Laboratory, Department of Civil and Environmental Engineering, University of California at Berkeley, Berkeley, CA 94720 USA (e-mail: sspark@berkeley.edu; smoura@berkeley.edu).

Dong Zhang is with the Department of Aerospace and Mechanical Engineering, The University of Oklahoma, Norman, OK 73019 USA (e-mail: dzhang@ou.edu).

Color versions of one or more figures in this article are available at https://doi.org/10.1109/TCST.2021.3135149.

Digital Object Identifier 10.1109/TCST.2021.3135149

Volumetric heat capacity for core (C_n) $C_{p/ps}$ and surface (C_{ps}) $(J \cdot m^{-3} \cdot K^{-1})$. Solid-phase diffusion coefficient ($m^2 \cdot s^{-1}$). D_s E_{Φ} Activation energy of variable Φ (J·mol⁻¹). Faraday's constant (= $96487C \cdot mol^{-1}$). Lithium exchange rate parameter (s^{-1}). Heat transfer coefficient ($W \cdot m^{-2} \cdot K^{-1}$). h Reaction rate constant $(A \cdot m^{2.5} \cdot mol^{-1.5})$. k_n Thermal conductivity $(W \cdot m^{-1} \cdot K^{-1})$. k_T LElectrode/separator thickness (m). Moles of lithium (mol). R_g Universal gas constant (=8.31 J·mol⁻¹·K⁻¹). R_f Film resistance $\Omega \cdot m^2$. R_s Particle radius (m). SoC State of charge. $T_{c/s}$ Core/surface temperature (K). Reference/ambient temperature (K). $T_{\rm ref}/\infty$

Greek Symbols:

 α_0 Apparent transfer coefficient.

 β Particle volume ratio.

 γ Input coefficient (m²·C⁻¹).

 ε_s Active material volume fraction.

ρ Material balance (slope) coefficient.

 σ Material balance (intercept) coefficient.

Superscripts:

/ Separator domain.

Negative electrode domain.

+ Positive electrode domain.

I. INTRODUCTION

ITHIUM-ION (Li-ion) batteries are one of the most common energy storage technologies. They are used all across the spectrum of battery applications, ranging from portable electronics to grid-scale storage systems. Two important factors limit even wider adoption of this technology presently. They are short life expectancy and long charging times, as identified by the U.S. Department of Energy (DOE) [1].

In the last decade, the improvement of Li-ion battery performance through advanced management algorithms has gained traction within the scientific community [2], [3]. One of its most important aspects is the charging process. The

1063-6536 © 2021 IEEE. Personal use is permitted, but republication/redistribution requires IEEE permission. See https://www.ieee.org/publications/rights/index.html for more information.

most widely used protocol for battery charging is the constant current/constant voltage (CCCV) [4]. Although very simple and widely used, the CCCV is an empirical approach [5], which can be quite conservative [2]. Indeed, the CCCV is unable to charge a battery while satisfying "by design" the electrochemical safety constraints associated with lithium plating notably. Constraint satisfaction is achieved only "in practice," by tuning the protocol in a conservative way. However, a tradeoff between constraint fulfillment and fast charging has to be found by an appropriate setting of the charging current.

In recent years, other fast charging schemes have been proposed in the scientific literature [6], [7]. Several approaches extend the CCCV protocol through multistage CC [8], boostcharging [9], and pulse charging [10], among others [11], [12]. Although these methods are improvements over CCCV, they suffer from the same limitations—they are heuristic methods that do not ensure constraint satisfaction "by design." Observe that, to handle electrochemical constraints "by design," one cannot use empirical models characterizing only the "external" electrical behavior of a battery but should base the design on an electrochemical model [2] (popular methods based on equivalent circuit models [13], [14] or data-driven approaches [15], [16] cannot be used here). Therefore, several approaches have been developed, which computes the optimal charging profile to ensure the satisfaction of electrochemical constraints. The optimality criteria often include the minimization of charging time [17], [18] and capacity fade [19], [20] or the maximization of charge stored at a given time instant [21] while accounting for constraints on solid- and electrolyte-phase concentrations [18], [22], temperature [18], [22], [23], intercalation-induced stresses [21], and lithium plating [17], [20], [23]. Although important from a theoretical viewpoint, the main limitation of these strategies is that they are open loop, i.e., no information on the current state of the battery (e.g., voltage, temperature, or SoC) is exploited to dynamically adjust the applied input current, which makes them susceptible to modeling uncertainties and varying initial SoC.

More recently, some closed-loop control schemes for fast and healthy charging have been proposed in the literature. By healthy, we mean that constraints are introduced in order to limit side reactions that induce accelerated aging. Healthy charging protocols thus aim at slowing down battery aging with respect to a given standard charging. The most common approaches in this regard are based on model predictive control (MPC). The first MPC scheme proposed for battery charging is [23], which makes use of the Doyle–Fuller–Newman (DFN) electrochemical model [24]. The main limit of this method is that the DFN model is a very complex nonlinear model based on partial differential equations (PDEs) [25] and subject to nonconvex constraints, which makes the resulting online optimization computationally challenging. A way to decrease this computational cost is to use reduced order [19], [26], [27] or reformulated [28] electrochemical models. MPC strategies based on such models have been proposed, for instance, in [22] and [28]-[32]. It must be noted that, even with a reduced linear model, MPC can still be computationally demanding

for embedded controllers typically associated with battery chargers. An alternative approach to MPC, which is computationally less demanding, is the reference governor (RG) approach. The first exploration of RGs for battery charging was carried out in [33]. In [34], a computationally low-cost RG was introduced, which, using a reduced-order electrochemical model, achieves fast charging while satisfying prescribed electrochemical constraints.

The present work builds upon the latter approach and it departs from previous works in the following ways: 1) a thermoelectrochemical model of the battery with time-varying film resistance (to account for electrolyte and aging dynamics) is identified and used for closed-loop controller design; 2) a closed-loop controller for fast healthy charging that is robust to temperature changes is designed; and 3) battery-in-theloop experiments and battery aging campaigns are used for validation. Notice that this is in stark contrast with other constraint-aware charging policies mentioned above where no such validation has been performed, leaving the claimed benefits of electrochemical model-based constrained control in Li-ion battery charging as a conjecture. Experimental aging campaigns are conducted in [16], [18], and [19], but a single optimal charging profile is computed offline at the beginning of battery life and fed to a battery throughout its entire lifetime, which falls in the open-loop charging methods.

This article is organized as follows. Section II deals with the modeling methodology for the Li-ion battery. The controller design is described in Section III, and the experimental procedure and results are presented and discussed in Sections IV and V, respectively.

II. MODELING METHODOLOGY

We introduce here the different aspects involved in the modeling and identification from experimental data of the electrochemical models considered in this work.

A. Li-Ion Battery Modeling

Li-ion batteries transform electrical energy into chemical energy during the charging process and vice versa when connected to a load. A battery is composed of three domains and two phases. The three domains are: 1) the positive electrode (+); 2) separator; and 3) negative electrode (-). The two phases are: 1) the electrolyte solution phase and 2) the porous solid phase. While the electrolyte phase covers both electrodes and separator domains, the solid phase is only present in the electrode domains. During battery charge, lithium is deintercalated (oxidation reaction) from the positive electrode solid phase. This lithium is then immersed in the electrolyte phase of the positive electrode in the form of Li-ions. These ions migrate from the positive electrode, through the separator, and to the negative electrode. Once there, lithium is intercalated (reduction reaction) into the negative electrode solid phase. Meanwhile, an electric current is generated and goes from the positive to the negative electrode. This completes the electrochemical charging process. These electrochemical phenomena are captured by the DFN model, which is based on the porous electrode and concentrated solution theories. It describes the porous solid phase of the electrode as a set of spherical particles of uniform size and considers that transport of Li-ions occurs in one dimension only. This model results in a set of PDEs that are algebraically coupled, as reported in [2] and [24], and extensions with thermal dynamics can be found in [26] and [35]. Such a DFN model with thermal dynamics (a simple two-state thermal model) is used in this article for control validation purposes.

The DFN model complexity makes its use more challenging when designing the charging feedback control law, which motivates the use of reduced-order electrochemical models, such as the equivalent hydraulic model (EHM). The EHM strikes a good balance between simplicity, accuracy, and interpretability. This model belongs to the single-particle model (SPM) class in which each electrode solid phase is represented by a single, suitably scaled, spherical particle. The model reduction from the DFN model to the EHM is based on the following assumptions. [36]:

- A1: The electrolyte dynamics are constant in space and time.
- A2: A single particle is used to represent each electrode.
- A3: The solid-phase diffusion coefficient is spatially independent.

Under Assumptions A1–A3, a transcendental transfer function for each solid-phase diffusion PDE is obtained [37]. These transfer functions can then be truncated through the Padé approximations of a given order [38]. A tank system can be shown to have a transfer function with similar structure as this Padé approximation, and the state-space model describing its physical behavior presents an analogy with the lithium diffusion process. This allows matching the coefficients of the EHM with electrochemical parameters and retaining a physical meaning for the state vector. More details can be found in [39].

Prior work has shown that a second-order approximation of the solid-phase electrode dynamics is adequate to represent battery dynamics [39]. Hence, the model consists of an integrator to determine the SoC combined with the dynamics of the electrode surface concentration. The resulting EHM takes the form

$$x(k+1) = A_{\mu}x(k) + B_{\mu}u(k) \tag{1}$$

where $x = [SoC, CSC]^T$ is the state vector consisting of the SoC of the battery and the critical surface concentration and u is the applied current, which is negative during charging. The state and input matrices are

$$A_{\mu} = \begin{bmatrix} \frac{1}{g} & 0 \\ \frac{1}{\beta(1-\beta)} & 1 - \frac{g}{\beta(1-\beta)} \end{bmatrix}, \quad B_{\mu} = \gamma \begin{bmatrix} \frac{1}{1} \\ \frac{1}{1-\beta} \end{bmatrix}$$
(2)

where index μ stands for the model parameters $\mu = [g, \gamma]^T$. The hydraulic parameters g, a valve coefficient, and γ , the input coefficient of the two-tank system, are respectively equivalent to the inverse of the diffusion time constant and the inverse of the electrode capacity (see Table I). Parameter $\beta = 7/10$ follows from the Padé truncation [39] and a sampling time of 1 s has been considered. This EHM represents the diffusion of lithium inside an electrode as diffusion of fluid in a two-tank system, and it is electrochemical coherent with other

TABLE I FUNCTIONS ASSOCIATED WITH THE BATTERY MODELS †

Func.	Function
g, γ	$rac{147}{20}rac{D_s}{R_s^2}, \; rac{1}{Larepsilon_s F c_{s, ext{max}}}$
$ ho,\sigma$	$-\frac{c_{s,\max}^{-}L^{-}\varepsilon_{s}^{-}}{c_{s,\max}^{+}L^{+}\varepsilon_{s}^{+}},\;\frac{n_{s}^{Li}}{c_{s,\max}^{+}L^{+}\varepsilon_{s}^{+}A}$
$h_{ heta}$	$\eta_s^+(x(k), u(k)) - \eta_s^-(x(k), u(k)) + h_\omega(x(k)) - R_f u(k)$
η_s^{\pm}	$\frac{R_g T_{\text{ref}}}{\alpha_0 F} \sinh^{-1} \left(\frac{\mp 1}{2a_s^{\pm} L^{\pm} j_{n,0}^{\pm}(x(k))} u(k) \right)$
$U^{\pm a} U^{\pm a}$	$k_n^{\pm} c_{s,\max}^{\pm} \sqrt{c_e} \sqrt{z(k) \left(1 - z(k)\right)}$
	same as in [41]
f_{μ}	$\begin{bmatrix} 1 & 0 \\ \frac{g(T_c(k))}{\beta(1-\beta)} & 1 - \frac{g(T_c(k))}{\beta(1-\beta)} \end{bmatrix} x_{ec}(k) + \left[\frac{\gamma}{\gamma} \right] u(k)$
f_{μ_T}	$\begin{bmatrix} 1 - \frac{k_T}{\rho_{\mathrm{avg}} C_p} & \frac{k_T}{\rho_{\mathrm{avg}} C_p} \\ \frac{k_T}{\rho_{\mathrm{avg}} C_{ps}} & 1 - \frac{\mathbf{h} + k_T}{\rho_{\mathrm{avg}} C_{ps}} \end{bmatrix} x_T(k) + \begin{bmatrix} -\frac{\varphi(x_{ec}(k))}{\rho_{\mathrm{avg}} C_p} u(k) \\ \frac{\mathbf{h}}{\rho_{\mathrm{avg}} C_{ps}} T_{\infty} \end{bmatrix}$
φ	$V(k) - (U^{+}(\rho \operatorname{SoC}(k) + \sigma) - U^{-}(\operatorname{SoC}(k)))$
Φ^b	$\Phi_{ m ref} \exp\left(rac{E_{\Phi}}{R_g}\left(rac{1}{T_{ m ref}}-rac{1}{T_c(k)} ight) ight)$
h_{ω}	$U^{+}(x(k)) - U^{-}(x(k))$
g_c	$a_{lp}\log(b_{lp}\mathrm{CSC}(k)) + c_{lp} - u(k)$

[†]Function arguments (column 1) are avoided to save space. ${}^az(k) = \rho \mathrm{SoC}(k) + \sigma$ for + and $z(k) = \mathrm{CSC}$ for -.

SPMs [36]. The dynamics of each electrode can be modeled by an EHM. However, the battery system consisting of two electrodes is well known to be unobservable [40]. This issue is alleviated by making some standard assumptions when considering the graphite/nickel–cobalt–aluminum (NCA) chemistry used in this article. We assume instantaneous dynamics in the NCA electrode (CSC+(k) \approx SoC+(k)) since its diffusion time constant is much smaller than the graphite one ($\tau^+ \approx 500~\text{s},$ $\tau^- \approx 7000~\text{s})$ and we exploit material balance to write the positive electrode dynamics as SoC+(k) = ρ SoC(k) + σ with ρ and σ grouping electrochemical parameters [39], as shown in Table I. Hence, an EHM (1) is required for the negative electrode only. The interested reader is referred to [39] for more details.

The associated output equation has the form

$$y_V(k) = h_\theta(x(k), u(k)) \tag{3}$$

where the output $y_V = V$ is the voltage across the battery characterized by the nonlinear function $h_\theta: \mathbb{R}^2 \times \mathbb{R} \to \mathbb{R}$, which is reported in Table I. The first two terms of this function are Butler–Volmer surface overpotentials for positive and negative electrodes, respectively, the third term is the difference between open circuit potentials of positive and negative electrodes, and the last term is a film resistance ohmic drop. The index θ refers to the parameter vector containing all the electrochemical parameters that characterize the considered function, such as material balance coefficients ρ and σ , maximum solid concentration of lithium $c_{s,\text{max}}$, and electrode thickness L, to name a few [39].

^bIn the Arrhenius law, Φ stands for g and k_n

This EHM in Eqs. (1), (3) is coupled with the same second-order thermal model and associated thermal parameters used in the DFN model. The thermal effects on the diffusion time constant 1/g are modeled by the Arrhenius law [35] as reported in Table I. This reduced-order coupled electrochemical/thermal model is denoted as temperature-dependent EHM (TEHM) and it takes the following form:

$$x_{\rm ec}(k+1) = f_{\mu}(x_{\rm ec}(k), x_T(k), \mu(k))$$
 (4)

$$x_T(k+1) = f_{\mu_T}(x_{ec}(k), x_T(k), u(k))$$
 (5)

where $x_{\rm ec}$ denotes the electrochemical state and x_T denotes the thermal state. They are defined as $x_{\rm ec} = [{\rm SoC}, {\rm CSC}]^{\rm T}$ and $x_T = [T_c, T_s]^{\rm T}$, where T_c, T_s are respectively the core and surface cell temperatures. The nonlinear functions f_μ : $\mathbb{R}^2 \times \mathbb{R}^2 \times \mathbb{R} \to \mathbb{R}^2$ and $f_{\mu_T} : \mathbb{R}^2 \times \mathbb{R}^2 \times \mathbb{R} \to \mathbb{R}^2$ are defined in Table I. While f_μ is the temperature-dependent version of the electrochemical subsystem (1), the temperature subsystem is specified by f_{μ_T} and it follows from thermal balance. The first equation in f_{μ_T} involves core-surface thermal conductivity and heat generation from Joule and entropic effects, and the second equation includes heat convection with the environment. The associated output equation is given by

$$y_{(V,T)}(k) = h_{(ec,T),\theta}(x_{ec}(k), x_T(k), u(k))$$
 (6)

where the output is $y_{(V,T)} = [V, T_s]^T$, which is characterized by the nonlinear function $h_{(ec,T),\theta} = [h_\theta, T_s]^T : \mathbb{R}^2 \times \mathbb{R}^2 \times \mathbb{R} \to \mathbb{R}^2$ with h_θ reported in Table I.

B. Model Identification

Both models used in this study, namely, the DFN model with thermal dynamics and the TEHM, needed to be identified from data coming from a graphite-anode/NCA-cathode cell. The parameters of the DFN model were fit using the procedure described in [41]. The currents used for identification consisted in a library of input profiles covering a wide range of frequency content and current magnitudes. The identified parameters were taken from [41]. Fig. 1(a) and (b) illustrate the good fit between the experimentally measured voltage and surface temperature with the DFN simulation model for a 2C constant current charging profile, resulting in root-mean-square errors (RMSEs) of 28 mV and 0.65 °C, respectively. This fit quality is comparable to others reported in the literature [41], [42].

To determine the unknown parameters in the TEHM (4)–(6), the two-step procedure described next is used.

Step 1 (Determination of Equilibrium and Diffusion-Related Dynamic Parameters): An estimate $\hat{\mu}$ of the parameter vector μ in (1) was deduced from the DFN model parameters estimated in [41] using the relations in Table I [39]: $g=10^{-3}$ s⁻¹ and $\gamma=6.50\times10^{-6}$ m² · C⁻¹. Similarly, an estimation $\hat{\theta}$ for the parameter vector θ in (3) was obtained from the identified DFN model, where $\rho=-0.76$ and $\sigma=0.90$. The obtained values for the remaining parameters in θ can be found in [41].

Step 2 (Estimation of Temperature-Related Dynamic Parameters): The parameter vector $\mu_T = [C_p, C_{ps}, h, k_T]^T$ of the thermal dynamics in (5) was estimated from a dataset

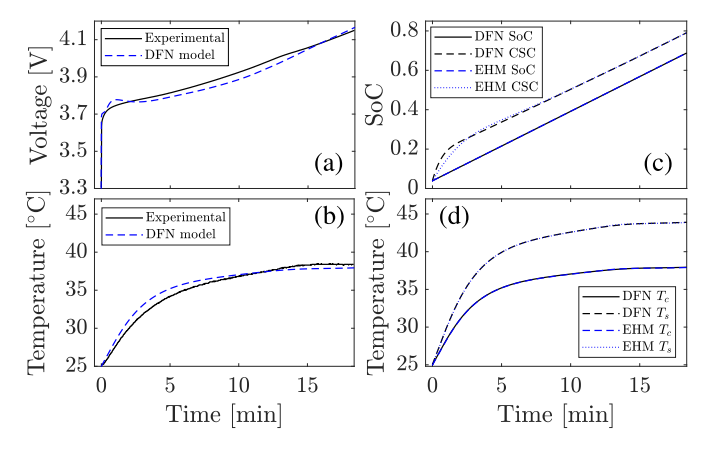


Fig. 1. Model comparisons between experimental measurements and the DFN model in terms of (a) voltage and (b) temperature and between the DFN model and the TEHM in terms of (c) solid-phase diffusion states (i.e., SoC and CSC) and (d) thermal states (i.e., core and surface temperatures).

recorded at high current (larger than 1C) 1 of N_T samples. In the following problem:

$$\min_{\mu_T} \sum_{i=1}^{N_T} (T_{s,T}(i) - T_s(i))^2$$
 (7)

s.t. equations
$$(4)$$
– (6) (8)

 T_s is the model output and $T_{s,T}$ is the measured signal. This problem was solved using the particle swarm optimization algorithm [43] in order to obtain the required parameter estimates. This algorithm benefits from handling nonlinear optimization problems with possibly multiple minima, efficiency, and simplicity in implementation [43]. The estimated parameters are $\hat{\mu}_T = [4.70 \times 10^2, 4.50, 2.17, 4.70]^T$ with units as $J \cdot m^{-3} \cdot K^{-1}$ for the first two vector components, $W \cdot m^{-2} \cdot K^{-1}$ for the third one, and $W \cdot m^{-1} \cdot K^{-1}$ for the last one.

Fig. 1 also compares the TEHM with the more complex DFN model, in the case of 2C charging. Fig. 1(c) shows the bulk SoC, which represents available energy, and the CSC, which represents available power. Fig. 1(d) shows core and surface temperature. Regarding the SoC, the indicator used here is the electrode stoichiometry defined as SoC = $c_s/c_{s,max}$, where c_s is the current lithium concentration and $c_{s,max}$ is the maximum lithium concentration of a given electrode. For reference, NCA cells have SoC = 0.93 at 4.2 V. Another popular SoC notion is based on the Coulomb counting (SoC_{cc}) defined as $SoC_{cc} = Q/Q_{nom}$, where Q and Q_{nom} are the current battery capacity and the one determined under nominal conditions, respectively. As comparison, $SoC_{cc} = 0\%$ yields SoC = 0, while $SoC_{cc} = 100\%$ corresponds to SoC = 0.93for a voltage range of [3.3, 4.2] V. Regarding CSC, there is a slight mismatch between the CSC of the EHM and the DFN at low SoCs, resulting in 1.2×10^{-2} RMSE (since the concentration is normalized, the RMSE is dimensionless) between the two models, which is due to the low-order approximation. However, this modeling gap is reduced at high SoCs, which is

¹C-rate: normalization of the battery current in A with respect to the battery nominal capacity in Ah.

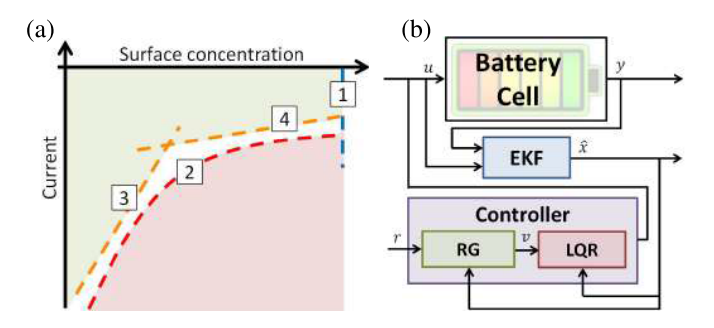


Fig. 2. Constraint-aware control scheme for Li-ion battery charging, where (a) feasible and infeasible operating regime in the CSC plane and (b) proposed feedback control scheme.

the most stringent operating region for constraint fulfillment and notably overcharge avoidance, as seen next. Overall, the curves for the TEHM model exhibit a good agreement with the curves obtained with the DFN simulator with RMSEs of 2.8×10^{-4} for SoC and 2.6×10^{-2} °C and 2.9×10^{-2} °C for core and surface temperature, respectively.

C. Degradation Constraints

The battery electrochemical state should be kept within specific operational constraints to avoid undesired electrochemical phenomena caused by side reactions. Some of the most relevant side reactions are electrode structural changes and lithium plating. The operational constraints considered here are shown in Fig. 2(a). The dashed blue line (constraint 1) delimits the upper bounds for SoC and critical surface concentration, which limits the maximum allowable concentration of lithium in the electrode. The red area delimited by the dashed red lines (constraint 2) is the region where lithium plating occurs. The complement region of the red zone corresponds to the operating conditions within which the battery charging is performed in a healthy fashion, and therefore, it denotes the safe operating area [44] of the battery in the electrochemical space. Lithium plating degrades the battery in two ways: 1) it consumes available lithium and 2) the lithium tends to form dendrites. Extreme conditions that promote lithium plating are charging at low temperature [45], [46] or high current rate [47], [48] which is especially aggravated for high SoC [47]. However, it has also been reported to occur at milder conditions, such as charge rates as low as about C/6 at 20 °C [47].

In the EHM, the threshold potential that induces lithium plating results in a static nonlinear inequality that is a function of the CSC and the charging current [see Fig. 2(a), constraint 2]. This threshold is obtained from the literature for the studied graphite/NCA cell [49], and the DFN simulator is used to draw the associated nonlinear function. The limits on both lithium plating and lithium concentration can be represented as model constraints that take the following mathematical form:

$$\begin{cases} x(k) \le \bar{x} & (9a) \\ g_c(x(k), u(k)) < 0 & (9b) \end{cases}$$

where \bar{x} is an upper bound on electrode lithium concentration preventing an excess of lithium to be deposited at the surface

of the electrode and $g_c: \mathbb{R}^2 \times \mathbb{R} \to \mathbb{R}$ is a nonlinear function that mitigates the effect of lithium plating. Function g_c is obtained by fitting a curve to the lithium plating boundary (negative electrode potential equal to zero) obtained from the simulation of the DFN model under different constant current charging conditions [34]. The expression for function g_c can be found in Table I, whereas the parameter values are given by $a_{lp}=1.74$, $b_{lp}=9.32$, and $c_{lp}=-4.46$.

III. CONTROLLER DESIGN METHODOLOGY

We now introduce the different aspects involved in the controller design and its validation in simulation.

A. Feedback Charging Control

In contrast to standard CCCV charging strategies or *a priori* computation of input profiles, closed-loop control provides the means to charge a battery to a given set point (e.g., 100% SoC) while ensuring that the internal states remain in the safe region. The latter feature is achieved by using a cascaded control structure [see the purple block in Fig. 2(b)] relying on the RG method in order to generate the charging current *u*. The inner and outer loops of the controller are as follows:

- a linear state feedback regulator [red block in Fig. 2(b)] that produces a current profile to aggressively charge the battery toward a SoC set point v;
- 2) an RG [green block in Fig. 2(b)] that generates the SoC set point v from a desired set point r and the battery state information x, where v serves as a virtual input to ensure constraint satisfaction.

A linear-quadratic regulator (LQR) is designed for the inner loop. It guarantees the asymptotic stability of the battery system (which is a marginally stable system). In order to keep a linear framework, and given that there are no stringent performance requirements on this inner loop, we will consider that the battery behavior is described by a polytopic uncertain system (1) and (2), in which g is seen as a time-varying parameter. This uncertainty accounts for possible deviations from isothermal conditions due to the fast charging control of the battery. For a temperature range between 0 °C and 45 °C and the considered chemistry, the range of values for g is $[2 \times 10^{-4}, 3 \times 10^{-3}]$. The controller design is performed in two stages. First, an LQR controller is designed for the nominal linear time-invariant model (1) corresponding to a temperature of 25 °C. This corresponds to the conditions in which parameter μ was estimated. Next, stability robustness is checked for the considered range of values for g via a common Lyapunov function.

The LQR is designed from the EHM (1) with $\mu=\hat{\mu}$. Besides, in order to ensure zero steady-state error with respect to the SoC set point v (and hence with respect to the desired set point r when constraints are fulfilled), an integrating action is added in the control law due to the following controller state equation:

$$x_i(k+1) = x_i(k) + (v(k) - Cx(k))$$
(10)

where $x_i \in \mathbb{R}$ is the state of the integrator, $v \in \mathbb{R}$ is the SoC reference, and $C = \begin{bmatrix} 1 & 0 \end{bmatrix}$ selects the SoC component of x.

The state feedback control law takes the form

$$u(k) = -[K \quad K_i] \begin{bmatrix} x(k) \\ x_i(k) \end{bmatrix} \stackrel{\triangle}{=} -K_c x_a(k). \tag{11}$$

The dynamics for the augmented state vector, x_a , are obtained by grouping (1) and (10), namely

$$x_a(k+1) = \begin{bmatrix} A_{\mu} & 0 \\ -C & 1 \end{bmatrix} x_a(k) + \begin{bmatrix} B_{\mu} \\ 0 \end{bmatrix} u(k) + \begin{bmatrix} 0 \\ 1 \end{bmatrix} v(k)$$
(12)

and the gain K_c in (11) is obtained by solving the following LQR problem:

$$\min_{u} \frac{1}{2} \sum_{k=0}^{\infty} x_{a}^{\mathsf{T}}(k) Q_{c} x_{a}(k) + u^{\mathsf{T}}(k) R_{c} u(k)$$
 (13)

In the above expression, $Q_c \succeq 0$ and $R_c \succ 0^2$ are design parameters.

Substituting (11) into (12) yields the closed-loop system

$$x_a(k+1) = A_{cl}x_a(k) + B_{cl}v(k)$$
 (15)

with

$$A_{\rm cl} = \begin{bmatrix} A_{\mu} - B_{\mu}K & -B_{\mu}K_i \\ -C & 1 \end{bmatrix} \text{ and } B_{\rm cl} = \begin{bmatrix} 0 \\ 1 \end{bmatrix}. \quad (16)$$

In order to give a guaranteed stability with respect to the variations of g, we proved the robustness of the provided control law. To do so, we denoted as $A_{\rm cl}^{\rm min}$ and $A_{\rm cl}^{\rm max}$ the closed-loop matrices for the minimum and maximum values of g, respectively. The resulting system can be seen as a polytopic uncertain system for which asymptotic stability can be proved by finding a common Lyapunov matrix P > 0 that ensures the satisfaction of the following linear matrix inequalities (LMIs):

$$\left(A_{\min}^{\text{cl}}\right)^{\text{T}} P A_{\min}^{\text{cl}} - P < 0 \tag{17}$$

$$\left(A_{\text{max}}^{\text{cl}}\right)^{\text{T}} P A_{\text{max}}^{\text{cl}} - P < 0. \tag{18}$$

B. Constraint Management

Although the LQR controller ensures closed-loop asymptotic stability, it is not able to satisfy the electrochemical constraints. To provide constraint-handling capabilities to the control scheme, we use an RG. An RG is a predictive control law that enforces constraint satisfaction by suitably manipulating the reference of a prestabilized system. The basic idea of any RG is to provide, at each sampling time t, a set point v that is as close as possible to the desired set point r [see Fig. 2(b)] and that, if kept constant from t onward, would not induce constraint violation. RGs are very computationally efficient when applied to linear systems subject to the intersection of linear convex constraints [50] such as inequality (9a). Unfortunately, in our case, one of the electrochemical constraints—lithium

plating inequality (9b)—is a nonlinear concave constraint [see Fig. 2(a)] that is not amenable to such efficient methods. Besides, it must be pointed out that the set boundary is subject to model uncertainty due to parameter uncertainties and the fact that we are approximating an infinite-dimensional model with a finite one.

To overcome these problems, we pursued the following approach: 1) we suitably restricted the constraints to ensure robustness against uncertainties and 2) we embedded the nonconvex constraint as the union of two linear constraints [see Fig. 2(a)]. The dashed orange lines denoted by 3 and 4 demark the safety margin, which accounts for model uncertainty and disturbances. The safe operating area is in green. With these considerations, we mathematically reformulated the constraints as the intersection of the union of regions given by

$$\bigwedge_{i=1}^{c_c} \bigvee_{i=1}^{n_{c,j}} \left(S_{j,i}^{\mathsf{T}} x_a(k) \le s_{j,i} \right) \tag{19}$$

where $c_c = 2$, $n_{c,1} = 1$, and $n_{c,2} = 2$. Vectors $S_{j,i}^{\rm T}$ and scalars $s_{j,i}$ are reported in Table II. In this way, the admissible area is obtained from the union of the region constrained by 3 and 4, intersected with the region constrained by 1, resulting ultimately in a nonconvex set.

Since no RG scheme is reported in the literature [50], [51] that is able to deal with OR constraints (i.e., union of constraints), a new scheme has been developed. As any RG, in line of principle, an OR-RG should solve the following optimization problem representing the problem of finding the closest applied reference v(t) to the desired reference r(t) (in our case, r(t) = 1) such that the constraints are satisfied over an infinite horizon, i.e.,

$$\kappa(k) = \max_{\kappa \in [0,1]} \kappa$$
s.t. $v(k) = v(k-1) + \kappa(r(k) - v(k-1))$

$$\bigwedge_{j=1}^{c_c} \bigvee_{i=1}^{n_{c,j}} S_{j,i}^{\mathrm{T}} \hat{x}_a(\ell | x_a(k), v(k)) \le s_{j,i}$$

$$l = 0, \dots, \infty$$

where $\hat{x}_a(\ell|x_a, v) = A_{\rm cl}^{\ell}x_a + (I - A_{\rm cl})^{-1}(I - A_{\rm cl}^{\ell})B_{\rm cl}v$ is the ℓ step-ahead prediction given the initial state x_a and applying the constant reference v. The new reference to be applied is $v(k) = v(k-1) + \kappa(k)(r(k) - v(k-1))$. Interestingly enough, by performing an ε -restriction of the steady-state references, it is possible to reformulate the above infinite horizon problem with a finite number of constraints as follows:

$$\kappa(k) = \max_{\kappa \in [0,1]} \kappa$$

$$\text{s.t.} \bigwedge_{\ell=0}^{\ell^*+1} \bigwedge_{j=1}^{c_c} \bigvee_{i=1}^{n_{c,j}} \left(\alpha_{j,i}^{\ell}(v(k-1), r(k)) \kappa \right)$$

$$\leq \beta_{i,i}^{\ell}(v(k-1), r(k))$$

where ℓ^* is a finite integer. The expression of the scalars $\alpha_{j,i}^{\ell}(v(k-1),r(k))$ and $\beta_{j,i}^{\ell}(v(k-1),r(k))$ is provided in Table II. Surprisingly, this formulation of the RG problem can be solved in an almost closed form using the algorithm

 $^{^2}X \succeq 0 \ (X \succ 0)$ indicates that matrix X is positive semidefinite (positive definite).

TABLE II $MATHEMATICAL \ EXPRESSIONS \ ASSOCIATED \ WITH \ THE \ RG$

Variable	Function
$\{\overline{r},a_{j,i},b_{j,i}\}$	$ar{r}_{\mathrm{SoC}} = ar{r}_{\mathrm{CSC}} = 0.93,$ $a_{5,1} = 170, \ b_{5,1} = -130, \ a_{5,2} = 100, \ b_{5,2} = -100$
$\{S_{j,i}^{\mathrm{T}},s_{j,i}\}$	$S_1 = -[1\ 0\ 0]^{\mathrm{T}}, \ S_2 = -S_1, \ S_3 = -[0\ 1\ 0]^{\mathrm{T}}, \ S_4 = -S_3, \ s_1 = 0, \ s_2 = \bar{r}_{\mathrm{SoC}}, \ s_3 = 0, \ s_4 = \bar{r}_{\mathrm{CSC}}$ where $S_{j,1} = S_j$ for $j = 1,, 4, \ S_{5,i}^{\mathrm{T}} = a_{5,i}[0\ 1\ 0] - [K - K_c], \ s_{5,i} = -b_{5,i}$ for $i = \{1, 2\}$
$\{H_x, H_v, h_0\}$	$\begin{bmatrix} SA_{cl}^{0} \\ SA_{cl}^{1} \\ SA_{cl}^{2} \\ SA_{cl}^{2} \\ \vdots \\ SA_{cl}^{\ell*} \\ 0 \end{bmatrix}, \begin{bmatrix} S(I - A_{cl})^{-1}(I - A_{cl}^{0})B_{cl} \\ S(I - A_{cl})^{-1}(I - A_{cl}^{1})B_{cl} \\ S(I - A_{cl})^{-1}(I - A_{cl}^{2})B_{cl} \\ \vdots \\ S(I - A_{cl})^{-1}(I - A_{cl}^{\ell*})B_{cl} \end{bmatrix}, \begin{bmatrix} s \\ s \\ s \\ \vdots \\ s(1 - \epsilon) \end{bmatrix}$
$\begin{cases} \alpha_{j,i}^{\ell}(v(k-1),r(k)),\\ \beta_{j,i}^{\ell}(v(k-1),r(k)) \end{cases}$	$\begin{split} H_{v,\ell,j,i}^{\mathrm{T}}(r(k)-v(k-1)), h_{0,j,i}-H_{x,\ell,j,i}^{\mathrm{T}}\mathbf{x}_{cl}(k)-H_{v,\ell,j,i}^{\mathrm{T}}v(k-1) \\ & \text{for } \ell=0,,\ell^*, \\ H_{v,j,i}^{\mathrm{T}}(r(k)-v(k-1)), h_{0,j,i}-H_{v,j,i}^{\mathrm{T}}v(k-1) \end{split}$

proposed in [34]. The resulting RG scheme ensures stability and recursive feasibility. The complexity of the proposed algorithm turns out to be linear in the number of states and constraints, which contrasts with MPC-based approaches for battery fast/healthy charging like [28] and [29] with cubic complexity. Other MPC implementations use computationally efficient algorithms such as the Hildreth algorithm [32], [52], but they still require to solve the MPC problem for a sequence of inputs, which is not the case for the RG that only looks for a scalar parameter by checking a set of inequalities. All this is reflected in a lower computational load for RG schemes than MPCs as reported in [53] for fast charging.

C. State Estimation

Note that the state feedback controller (11) cannot be implemented alone because the electrochemical states are not directly measurable. Therefore, a state observer [blue block in Fig. 2(a)] is introduced to determine a state estimate \hat{x} from the available system input current u and measured outputs (voltage and surface temperature) y on the basis of the model TEHM in (4)–(6). Since the TEHM is nonlinear, an extended Kalman filter (EKF) [54] is used. Indeed, the EKF has been successfully applied to Li-ion batteries for a long time [55], [56]. It strikes a good balance between algorithmic complexity and estimation accuracy and its stochastic stability properties have been analyzed elsewhere [57].

Let us rewrite (4) and (5) as

$$x(k+1) = f(x(k), u(k)) + w_x(k)$$
 (20)

where $f = [f_{\mu}, f_{\mu_T}]^T : \mathbb{R}^4 \times \mathbb{R} \to \mathbb{R}^4$, the state vector is $x = [x_{\text{ec}}^T, x_T^T]^T \in \mathbb{R}^4$, and w_x is the process noise. The output equation (6) can be rewritten as

$$y(k) = h(x(k), u(k)) + v_y(k)$$
 (21)

where the nonlinear output function is given by $h = h_{(ec,T),\theta}$. The process noise $w_x(k)$ and measurement noise $v_y(k)$ are two mutually uncorrelated zero-mean white noise sequences. Their

variance matrices Q and R will be used as design parameters for the EKF. Model (20) is complemented with the following state equation:

$$R_f(k+1) = R_f(k) + w_R(k)$$

modeling the time-varying film resistance. This extra state improves the quality of the state estimate, and it has been used in other research works [58], [59]. It captures unmodeled dynamics, e.g., diffusion dynamics in the electrolyte or solid electrolyte interphase. An EKF, as described in [60] for instance, has been implemented on the basis of this model. The numerical values for matrices Q and R are

$$Q = diag(10^{-13}, 10^{-11}, 10^{-9}, 10^{-9}, 10^{-5})$$

 $R = diag(10^{-6}, 10^{-4}).$

The initial state estimate \hat{x}_0 was set to

$$\hat{x}_0 = [[3.89, 3.89] \times 10^{-2}, [2.98, 2.98] \times 10^2, 1.84 \times 10^{-3}]^T$$
 and the associated variance P_0 was set to

$$P_0 = \text{diag}(10^{-9}, 10^{-9}, 10^{-5}, 10^{-5}, 10^{-1}).$$

The first two components of the state vector are unitless, while the second two components have units of K and the last one is $\Omega \cdot m^2$. The units of Q and P_0 appropriately follow from x_0 , and the ones for R accordingly follow from the ones of the output measurements, i.e., V and K.

The EKF's performance is shown in Fig. 3(b)–(d) for data generated with the thermo-DFN model simulator corresponding to a 2C constant current charge profile. The estimated SoC, CSC [Fig. 3(b)], core temperature [Fig. 3(c)], and estimated outputs [surface temperature in Fig. 3(c) and voltage in Fig. 3(d)] almost perfectly coincide with the simulator signals after initial transients, and most of the errors occur at the beginning of charge when the SoC is low. Therefore, critical regions at higher SoCs where electrochemical constraints are more stringent (less leeway for the input current) exhibit small modeling errors.

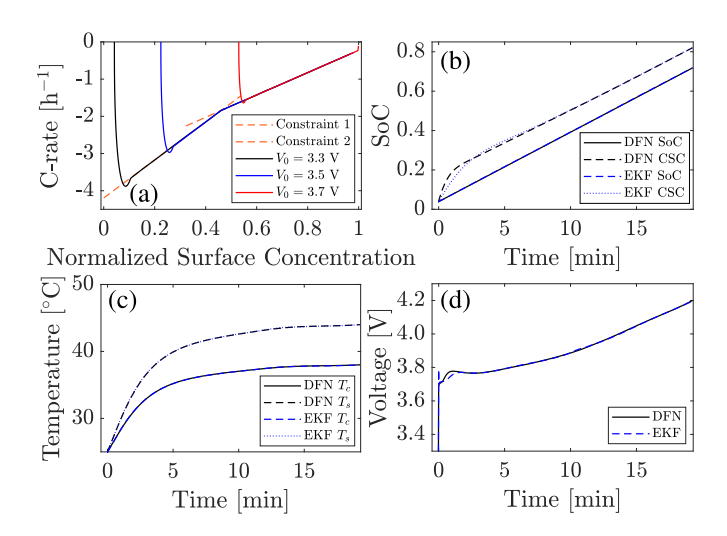


Fig. 3. Validation in simulation of the proposed EKF and closed-loop charging scheme. (a) Current-critical surface concentration (CSC) plane with linear lithium plating constraints (dashed orange lines), along with three closed-loop current-CSC trajectories for three different initial conditions. Performance of the TEHM-based EKF for (b) solid-phase diffusion states (i.e., SoC and CSC), (c) thermal states (i.e., core and surface temperatures), and (d) voltage.

D. Validation of the Control Scheme in Simulation

Before experimentally validating the performance of the proposed control scheme for battery charging, we evaluate it in simulation. The LQR design parameters Q_c and R_c in (13) are chosen so that the first term in (13) is weighted more than the second one in order to achieve fast closed-loop dynamics while guaranteeing stability robustness to changes in parameter g in the above indicated range. Matrix $Q_c = 100I_3$, while $R_c = 10^{-3}$. The design parameters for the EKF are the same as in Section III-C.

The simulation results of the closed-loop system are shown in Fig. 3(a), using the thermo-DFN model as a virtual battery cell. The figure portrays state trajectories in the current-CSC plane for three arbitrary initial voltages, namely, 3.3, 3.5, and 3.7 V (SoCs from 5% to 50%). From the figure, it follows that the closed-loop system reaches the constraints very quickly whatever the initial state, in accordance with the control scheme tuning highlighted above. Furthermore, the trajectory of the state complies with the linear constraints ascribed to lithium plating. Thus, the closed-loop control of the battery allows for arbitrary initialization, which cannot be achieved with open-loop charging methods.

IV. EXPERIMENTAL PROCEDURE

The experiments were carried out using Panasonic 2.7 Ah 18650 lithium NCA oxide battery cells.³ The experimental setup consists of a PEC Corporation SBT2050 series battery tester, an Espec BTX-475 environmental chamber, and a MicroAutoBox II 1401/1501 dSPACE card. Battery

³This type of cell has been used in the Tesla model S electric cars, for instance. Other types include Samsung prismatic nickel-manganese-cobalt (NMC) of BMW i3 [61], [62], LG Chem pouch NMC-lithium-manganese-oxide (LMO) of Chevy Volt [62], and AESC pouch NMC of Nissan Leaf [61] whose capacities exceed 50 Ah and can go up to 100+ Ah. The proposed RG scheme can be adapted to such large-format batteries by properly modeling them.

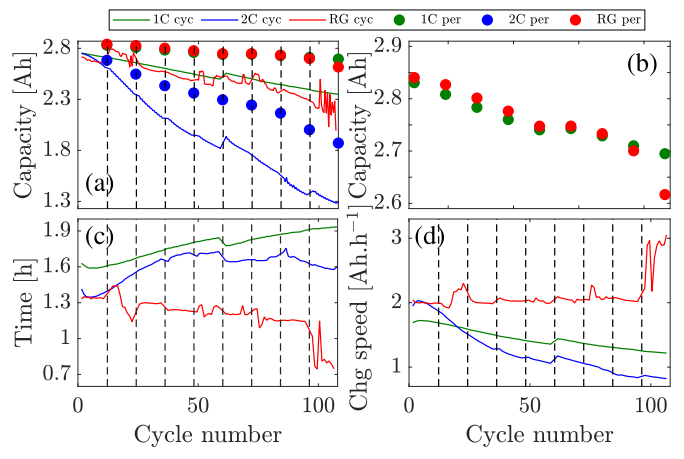


Fig. 4. Performance comparison between two CCCV strategies and the proposed RG charging strategy. (a) Retained capacity and (b) zoomed-in view of measured capacity for 1C and RG, (c) charge time, and (d) charge (chg) speed, all as a function of the cycle number.

measurements (current, voltage, and surface temperature) were collected each second. The temperature set point of the environmental chamber was set to $25~^{\circ}$ C.

Three charging strategies were tested, namely, 1C CCCV, 2C CCCV, and the proposed RG scheme. We used CCCV as a benchmark due to its wide use in the battery and electric vehicle industries [63], given its simplicity and low cost of implementation. The battery aging campaigns consisted of two tests, namely, a cycling test and a performance test. The first test consists of 11 charge/discharge cycles with four steps each. The first step is battery charging, which changes according to the studied strategy (1C CCCV, 2C CCCV, or RG with OR constraints). The second and fourth steps are 30-min resting periods. In the third step, the battery undergoes discharge using the same 1C CC policy for all scenarios. Next, a performance test is carried out to measure the charge capacity of the battery. It consists of two cycles with four steps each. As with the cycling tests, the second and fourth steps are resting periods. For the performance tests, both charge (first step) and discharge (third step) are executed with the 1C CCCV protocol. Both cycling and performance tests are consecutively repeated nine times.

V. RESULTS AND DISCUSSION

The desired SoC set point is 100%, which contrasts with other fast charging studies with 80% target SoC [16], [64]. By setting a lower reference, these fast charging studies avoid possibly high SoC degradation at the expense of oversizing the battery by 20%. The 100% battery charge is useful for applications such as mobile phones, laptops, and drones that provide the maximum possible autonomy to the user in a single charge, while other applications that benefit from recharging during operation (c.f., regenerative breaking in electric vehicles) can also extend their usage range by adding effective charge capacity on top of the one that can be gained during operation. Even if we considered full charge and CC full discharge cases, the proposed control scheme can be applied to any battery condition.

The performance of the three considered strategies is reported in Fig. 4(a) and (c) for capacity fade and charging time, respectively, where green and blue colors are ascribed to 1C CCCV and 2C CCCV, respectively, and the RG method is in red. Both cycling tests (curves denoted with cyc) and performance tests (symbols denoted with per) are shown in Fig. 4(a). The cycling tests include charge and discharge cycles, while only discharge cycles are considered for the performance tests. The temporal occurrence of performance tests is marked with black dashed vertical lines. Notice that the capacity measured during performance tests is larger than the one during cycling, which is expected due to the different current rates considered for each test. Moreover, there is cycling capacity recovery [65] after each performance test, which is also standard. Fig. 4(a) shows that the RG ages the battery similar to 1C and much less than 2C, respectively, 5% and 30% after 88 cycles.⁴ If we now look closer at the performance test [Fig. 4(b)], up to the seventh test, the RG degrades the battery consistently less than 1C. Note, however, that around the eighth and ninth performance tests, the RG exhibits some anomalous behavior, which degrades the capacity beyond the 1C strategy. This is arguably due to the fact that aging induces changes in the model parameters and thus in closed-loop dynamics; yet, at the present stage, the implemented control scheme does not adapt to such parametric changes. We decided to end the tests at this stage and further investigations are needed to validate this hypothesis. On the other hand, in terms of charging time, the RG systematically outperforms both 1C and 2C [see Fig. 4(c) showing the results cycle by cycle]. The RG takes 80 min at the beginning of life and 75 min on average over 88 cycles. Compare this to 2C, which initially charges in 85 min and 96 min on average. The times for 1C are even longer (98 and 106 min). Thus, the RG charges faster than 2C yet ages the cell similar to C/2 and 1C.

It is noteworthy that after 50 cycles, the RG stores more charge in less time than 2C. This fact is highlighted by looking at the charging speed, i.e., the amount of charge stored per unit of time, in Fig. 4(d) depicted in a cycle basis.

To further investigate how the RG achieves improved performance, we report the typical charging current profiles for the three protocols, as well as the resulting voltage and surface temperature. Fig. 5(a)–(c) shows the measured trajectories for the second charge (i.e., after transient) during the first cycling test of 1C CCCV, 2C CCCV, and RG charging strategies, with green dashed, blue dotted, and red solid curves associated with 1C, 2C, and RG, respectively.⁵ In Fig. 5(a) one can see that the RG imposes a high initial current spike of approximately 3C that lasts for a short time. In contrast, the CCCV current profiles have a step-like character, followed by a long decay during the CV charging phase. Recall that the RG generates a current profile by following the electrochemical constraints,

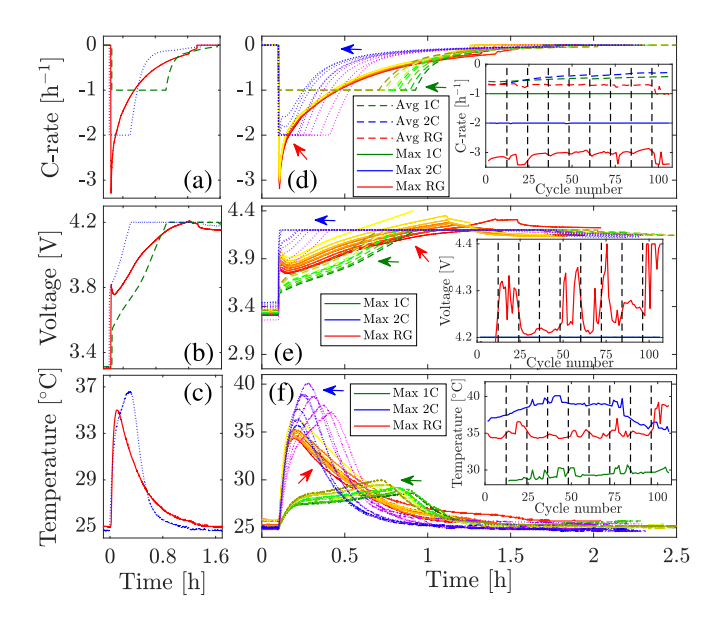


Fig. 5. Charge/discharge profiles of the two CCCV and the proposed RG charging strategies, and their aging evolution and associated stress factors influencing battery life. (a) Current, (b) voltage, and (c) surface temperature profiles during the second charge cycle for each charging strategy. (d)–(f) Aging evolution of each signal during the fifth cycle of each cycling test, i.e., each curve is separated by 11 cycles. The figure insets portray the common stress factors considered for Li-ion batteries per cycle number, namely, maximum (solid curves) and average (dashed curves) applied current, maximum terminal voltage, and maximum surface temperature.

and its fast charging capabilities can be related to the resulting profile. The obtained profile is the maximum current that can be given to the considered battery without violating lithium plating constraints notably.

As the battery ages, the current, voltage, and temperature trajectories change, as shown in Fig. 5(d)-(f) for 1C (green-olive dashed curves), 2C (pink-blue dotted curves), and RG (red-yellow solid curves). The color gradient and arrows indicate the first-to-last cycling tests. Note that the CC phases for 1C and 2C are shortened by 13 and 18 min, respectively, from the 5th to the 93th cycle, whereas the CV phase is enlarged by approximately 33 min for both charging strategies around the same cycle numbers [Fig. 5(d)and (e)]. This fact extends the charging time with battery usage. These issues are less pronounced for the RG [Fig. 5(d)], which explains the steady charging speed in Fig. 4(c). While the voltage response shows that the RG reaches higher voltages as the battery ages [Fig. 5(e)], the 2C strategy results in the highest surface temperature [Fig. 5(f)]. It is known that accelerated degradation is caused by a series of stress factors, including high currents and temperatures as well as extreme voltages [67]–[69]. In order to assess the impact of such factors in battery aging, insets of Fig. 5(d)–(f) show the maximum values of current, voltage, and temperature for 1C (green), 2C (blue), and RG (red). For CCCV charging strategies, the maximum current is the CC stage current, the average current includes the CV stage, and the maximum voltage coincides with the CV stage voltage of 4.2 V within a 1 mV of difference. The RG current averages to 0.7C over all the aging tests with a peak of 3C. This contrasts with averages of 0.4C and 0.3C for 1C and 2C CCCV, respectively [inset

⁴Cycle life of less than 100 cycles for 2C charging might seem extremely low. Just to put it into context, the used NCA cell is a conventional electric vehicle cell (energy optimized) with C/2 rated charging current, under which approximately 6% of capacity is lost after 88 cycles and the end-of-life (i.e., 80% capacity) is reached at 500 cycles [66].

⁵Given a problem with a thermocouple, the surface temperature for 1C could not be recorded for this cycling test.

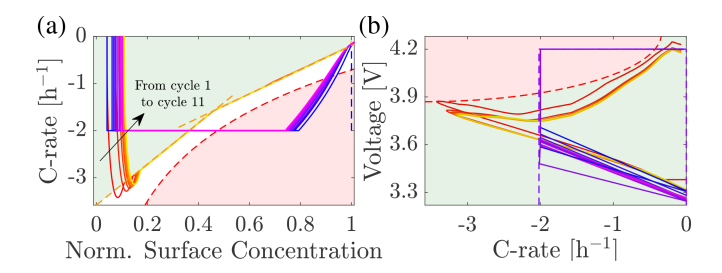


Fig. 6. State trajectories under the RG charging scheme (in red-to-yellow curves) and the 2C CCCV commercial charging strategy (in blue-to-magenta curves) in (a) CSC plane and (b) voltage–current plane (color gradient reflects cycle number from cycle 1 to 11). Classical CCCV box constraints as dotted purple rectangle versus novel safe operating area in green area.

of Fig. 5(d)]. These data explain how the RG consistently achieves faster charge times. The RG also allows voltages beyond the typical upper cutoff limit used by CCCV strategies, as evidenced in the inset of Fig. 5(e). Although the RG goes beyond the voltage limit of CCCV, it explicitly ensures that the internal states remain within a safe operating area. This can be seen in the CSC plane in Fig. 6(a), demonstrating that relevant electrochemical constraints are not violated when the RG is used. This fact contrasts with the CCCV design, which constrains the measured outputs [see the voltage-current plane in Fig. 6(b)] but violates electrochemical constraints [such as in CSC plane in Fig. 6(a)]. This argument explains how the RG achieves faster charge times without accelerating degradation. Finally, the RG achieves a maximum temperature of 35 °C compared to 40 °C for 2C and 30 °C for 1C [inset of Fig. 5(f)]. Note that the RG allows higher currents and voltages, yet the peak surface temperature is maintained below the 2C protocol's peak temperature—more than 2 °C—(except after cycle 97). Higher temperatures yield faster intercalation and reaction kinetics. Thus, high temperatures accelerate the main reaction but also accelerate side reactions. Consequently, temperature should be judiciously managed to enable faster charging without unduly accelerating degradation. The experiments demonstrate how the RG strikes a balance between the two CCCV schemes.

VI. CONCLUSION

The experimental results presented in this article demonstrate how a feedback control strategy outperforms traditional logic-based CCCV charging strategies in terms of capacity fade (26% less) and charging time (22% faster). Today, the de facto fast charging approach is based on limiting measured values, e.g., current, voltage, and temperature. Yet, these limits are proxies for the internal electrochemical states that directly govern charging and degradation. By using a (reduced) electrochemical model, the RG achieves shorter charge times with limited degradation by explicitly limiting the internal states within the safe operating area. The RG is based on electrochemical variables rather than just measured variables. The observations in Fig. 6, coupled with the fact that 2C CCCV rapidly degrades the battery after 88 cycles (70% of initial capacity for 2C CCCV compared to the 95% of the RG scheme), motivates switching the safe operating area from the purple dashed box to the green area in Fig. 6(b) in the traditional voltage-current plane.

It should be mentioned that the hypothesis of lithium plating as the main degradation mechanism taking place here would require validation through specific experiments (e.g., [48], [70]-[72], to name a few). Moreover, other degradation mechanisms might be triggered through the use of RG charging, which should also be determined. However, the results show that constraining plating with the RG during fast charging does increase the battery lifetime compared to the CCCV, which happens to violate such constraints. Moreover, consecutive CC and CV charging phases are, in general, not convenient for fast charging as batteries age. CC charging causes excessively high temperatures, while the CV phase becomes very long as the battery degrades. The RG-based charging strategy explicitly models degradation constraints and thus provides more aggressive (higher currents and voltages) yet healthier (lower temperatures and less aging) solutions for healthy fast charging.

REFERENCES

- Vehicle Technologies Office, Annual Merit Review, U.S. Department of Energy, Arlington, VA, USA, Jun. 2018.
- [2] N. A. Chaturvedi, R. Klein, J. Christensen, J. Ahmed, and A. Kojic, "Algorithms for advanced battery-management systems," *IEEE Control Syst. Mag.*, vol. 30, no. 3, pp. 49–68, Jun. 2010.
- [3] S. J. Moura and H. Perez, "Better batteries through electrochemistry," ASME Dyn. Syst. Control Mag., vol. 136, no. 6, pp. 15–21, Mar. 2014.
- [4] J. A. Carcone, "Performance of lithium-ion battery systems," in *Proc. WESCON*, Anaheim, CA, USA, 1994, pp. 242–248.
- [5] P. Keil and A. Jossen, "Charging protocols for lithium-ion batteries and their impact on cycle life—An experimental study with different 18650 high-power cells," J. Energy Storage, vol. 6, pp. 125–141, May 2016.
- [6] Y. Gao, X. Zhang, Q. Cheng, B. Guo, and J. Yang, "Classification and review of the charging strategies for commercial lithium-ion batteries," *IEEE Access*, vol. 7, pp. 43511–43524, 2019.
 [7] A. Tomaszewska *et al.*, "Lithium-ion battery fast charging: A review,"
- [7] A. Tomaszewska *et al.*, "Lithium-ion battery fast charging: A review," *eTransportation*, vol. 1, Aug. 2019, Art. no. 100011.
- [8] S. S. Zhang, "The effect of the charging protocol on the cycle life of a Li-ion battery," *J. Power Sources*, vol. 161, no. 2, pp. 1385–1391, Oct. 2006.
- [9] P. H. L. Notten, J. H. G. Op het Veld, and J. R. G. van Beek, "Boostcharging Li-ion batteries: A challenging new charging concept," *J. Power Sources*, vol. 145, no. 1, pp. 89–94, 2005.
- [10] A. Aryanfar, D. Brooks, B. V. Merinov, W. A. Goddard, A. J. Colussi, and M. R. Hoffmann, "Dynamics of lithium dendrite growth and inhibition: Pulse charging experiments and Monte Carlo calculations," *J. Phys. Chem. Lett.*, vol. 5, no. 10, pp. 1721–1726, 2014.
- [11] G. Sikha, P. Ramadass, B. S. Haran, R. E. White, and B. N. Popov, "Comparison of the capacity fade of Sony U.S. 18650 cells charged with different protocols," *J. Power Sources*, vol. 122, no. 1, pp. 67–76, Jul. 2003.
- [12] D. Anseán, M. González, J. C. Viera, V. M. García, C. Blanco, and M. Valledor, "Fast charging technique for high power lithium iron phosphate batteries: A cycle life analysis," *J. Power Sources*, vol. 239, pp. 9–15, Oct. 2013.
- [13] M. A. Xavier and M. S. Trimboli, "Lithium-ion battery cell-level control using constrained model predictive control and equivalent circuit models," *J. Power Sources*, vol. 285, pp. 374–384, Jul. 2015.
- [14] C. Zou, X. Hu, Z. Wei, and X. Tang, "Electrothermal dynamics-conscious lithium-ion battery cell-level charging management via state-monitored predictive control," *Energy*, vol. 141, pp. 250–259, Dec. 2017.
- [15] S. Park et al., "Reinforcement learning-based fast charging control strategy for Li-ion batteries," in Proc. IEEE Conf. Control Technol. Appl. (CCTA), Aug. 2020, pp. 100–107.
- [16] P. M. Attia *et al.*, "Closed-loop optimization of fast-charging protocols for batteries with machine learning," *Nature*, vol. 578, no. 7795, pp. 397–402, Feb. 2020.
- [17] J. Liu, G. Li, and H. K. Fathy, "A computationally efficient approach for optimizing lithium-ion battery charging," J. Dyn. Syst., Meas., Control, vol. 138, no. 2, Feb. 2016, 021009.

- [18] H. E. Perez, S. Dey, X. Hu, and S. J. Moura, "Optimal charging of li-ion batteries via a single particle model with electrolyte and thermal dynamics," *J. Electrochem. Soc.*, vol. 164, no. 7, pp. A1679–A1687, 2017.
- [19] M. Pathak, D. Sonawane, S. Santhanagopalan, R. D. Braatz, and V. R. Subramanian, "Analyzing and minimizing capacity fade through optimal model-based control-theory and experimental validation," ECS Trans., vol. 75, no. 23, pp. 51–75, 2017.
- [20] A. Pozzi, M. Torchio, and D. M. Raimondo, "Film growth minimization in a Li-ion cell: A pseudo two dimensional model-based optimal charging approach," in *Proc. Eur. Control Conf. (ECC)*, Limassol, Cyprus, Jun. 2018, pp. 1753–1758.
- [21] B. Suthar, P. W. C. Northrop, R. D. Braatz, and V. R. Subramanian, "Optimal charging profiles with minimal intercalation-induced stresses for lithium-ion batteries using reformulated pseudo 2-dimensional models," *J. Electrochem. Soc.*, vol. 161, no. 11, pp. F3144–F3155, 2014.
- [22] C. Zou, X. Hu, Z. Wei, T. Wik, and B. Egardt, "Electrochemical estimation and control for Lithium-ion battery health-aware fast charging," *IEEE Trans. Ind. Electron.*, vol. 65, no. 8, pp. 6635–6645, Aug. 2018.
- [23] R. Klein, N. A. Chaturvedi, J. Christensen, J. Ahmed, R. Findeisen, and A. Kojic, "Optimal charging strategies in lithium-ion battery," in *Proc. Amer. Control Conf.*, San Francisco, CA, USA, Jul. 2011, pp. 382–387.
- [24] J. Newman and K. Thomas-Alyea, Electrochemical Systems, 3rd ed. Hoboken, NJ, USA: Wiley, 2004.
- [25] K. A. Smith, C. D. Rahn, and C.-Y. Wang, "Model-based electrochemical estimation and constraint management for pulse operation of lithium ion batteries," *IEEE Trans. Control Syst. Technol.*, vol. 18, no. 3, pp. 654–663, May 2010.
- [26] C. Zou, C. Manzie, and D. Nešić, "A framework for simplification of PDE-based lithium-ion battery models," *IEEE Trans. Control Syst. Technol.*, vol. 24, no. 5, pp. 1594–1609, Sep. 2016.
- [27] R. D. Perkins, A. V. Randall, X. Zhang, and G. L. Plett, "Controls oriented reduced order modeling of lithium deposition on overcharge," *J. Power Sources*, vol. 209, pp. 318–325, Jul. 2012.
- [28] S. Kolluri, S. V. Aduru, M. Pathak, R. D. Braatz, and V. R. Subramanian, "Real-time nonlinear model predictive control (NMPC) strategies using physics-based models for advanced lithium-ion battery management system (BMS)," *J. Electrochem. Soc.*, vol. 167, no. 6, Jan. 2020, Art. no. 063505.
- [29] J. Liu, G. Li, and H. K. Fathy, "An extended differential flatness approach for the health-conscious nonlinear model predictive control of lithium-ion batteries," *IEEE Trans. Control Syst. Technol.*, vol. 25, no. 5, pp. 1882–1889, Sep. 2017.
- [30] M. Torchio, L. Magni, R. D. Braatz, and D. M. Raimondo, "Design of piecewise affine and linear time-varying model predictive control strategies for advanced battery management systems," *J. Electrochem.* Soc., vol. 164, no. 4, pp. A949–A959, 2017.
- [31] A. Pozzi, M. Zambelli, A. Ferrara, and D. M. Raimondo, "Balancing-aware charging strategy for series-connected lithium-ion cells: A non-linear model predictive control approach," *IEEE Trans. Control Syst. Technol.*, vol. 28, no. 5, pp. 1862–1877, Sep. 2020.
- [32] M. A. Xavier, A. K. de Souza, K. Karami, G. L. Plett, and M. Scott Trimboli, "A computational framework for lithium ion cell-level model predictive control using a physics-based reduced-order model," *IEEE Control Syst. Lett.*, vol. 5, no. 4, pp. 1387–1392, Oct. 2021.
- [33] H. Perez, N. Shahmohammadhamedani, and S. Moura, "Enhanced performance of li-ion batteries via modified reference governors and electrochemical models," *IEEE/ASME Trans. Mechatronics*, vol. 20, no. 4, pp. 1511–1520, Aug. 2015.
- [34] R. Romagnoli, L. D. Couto, A. Goldar, M. Kinnaert, and E. Garone, "A feedback charge strategy for li-ion battery cells based on reference governor," J. Process Control, vol. 83, pp. 164–176, Nov. 2019.
- [35] J. Mao, W. Tiedemann, and J. Newman, "Simulation of li-ion cells by dualfoil model under constant-resistance load," ECS Trans., vol. 58, no. 48, pp. 71–81, Apr. 2014.
- [36] S. J. Moura, N. A. Chaturvedi, and M. Krstić, "Adaptive partial differential equation observer for battery state-of-charge/state-of-Health estimation via an electrochemical model," *J. Dyn. Syst., Meas., Control*, vol. 136, no. 1, Jan. 2014.
- [37] T. Jacobsen and K. West, "Diffusion impedance in planar, cylindrical and spherical symmetry," *Electrochim. Acta*, vol. 40, no. 2, pp. 255–262, Feb. 1995.
- [38] J. C. Forman, S. Bashash, J. L. Stein, and H. K. Fathy, "Reduction of an electrochemistry-based li-ion battery model via quasi-linearization and Padé approximation," *J. Electrochem. Soc.*, vol. 158, no. 2, pp. A93–A101, 2011.

- [39] L. D. Couto, J. Schorsch, M. M. Nicotra, and M. Kinnaert, "SoC and SOH estimation for Li-ion batteries based on an equivalent hydraulic model. Part I: SoC and surface concentration estimation," in *Proc. Amer. Control Conf. (ACC)*, Boston, MA, USA, Jul. 2016, pp. 4022–4028.
- [40] D. Di Domenico, A. Stefanopoulou, and G. Fiengo, "Lithium-ion battery state of charge and critical surface charge estimation using an electrochemical model-based extended Kalman filter," J. Dyn. Syst., Meas., Control, vol. 132, no. 6, p. 061302, 2010.
- [41] S. Park, D. Kato, Z. Gima, R. Klein, and S. Moura, "Optimal experimental design for parameterization of an electrochemical lithium-ion battery model," *J. Electrochem. Soc.*, vol. 165, no. 7, pp. A1309–A1323, 2018.
- [42] C.-H. Chen, F. Brosa Planella, K. O'Regan, D. Gastol, W. D. Widanage, and E. Kendrick, "Development of experimental techniques for parameterization of multi-scale lithium-ion battery models," *J. Electrochem. Soc.*, vol. 167, no. 8, Jan. 2020, Art. no. 080534.
- [43] S. Ebbesen, P. Kiwitz, and L. Guzzella, "A generic particle swarm optimization MATLAB function," in *Proc. Amer. Control Conf. (ACC)*, Montreal, QC, Canada, Jun. 2012, pp. 1519–1524.
- [44] D. Andrea, Battery Management Systems for Large Lithium Ion Battery Packs. Norwood, MA, USA: Artech House, 2010.
- [45] T. Waldmann, M. Wilka, M. Kasper, M. Fleischhammer, and M. Wohlfahrt-Mehrens, "Temperature dependent ageing mechanisms in Lithium-ion batteries—A post-mortem study," *J. Power Sources*, vol. 262, pp. 129–135, Sep. 2014.
- [46] M. Petzl, M. Kasper, and M. A. Danzer, "Lithium plating in a commercial lithium-ion battery—A low-temperature aging study," *J. Power Sources*, vol. 275, pp. 799–807, Feb. 2015.
- [47] S. Ahmed et al., "Enabling fast charging—A battery technology gap assessment," U.S. Department of Energy, Idaho Nat. Lab., Falls, ID, USA, Tech. Rep. INL/JOU-17-41856, 2017.
- [48] U. R. Koleti, T. Q. Dinh, and J. Marco, "A new on-line method for lithium plating detection in lithium-ion batteries," *J. Power Sources*, vol. 451, Mar. 2020, Art. no. 227798.
- [49] P. Arora, M. Doyle, and R. E. White, "Mathematical modeling of the lithium deposition overcharge reaction in lithium-ion batteries using carbon-based negative electrodes," *J. Electrochem. Soc.*, vol. 146, no. 10, pp. 3543–3553, 1999.
- [50] K. Ilya and E. G. Gilbert, "Theory and computation of disturbance invariant sets for discrete-time linear systems," *Math. Problems Eng.*, vol. 4, no. 4, pp. 317–367, 1998.
- [51] E. Garone, S. Di Cairano, and I. V. Kolmanovsky, "Reference and command governors for systems with constraints: A survey on theory and applications," *Automatica*, vol. 75, pp. 306–328, Jan. 2017.
- [52] M. A. Xavier, "Efficient strategies for predictive cell-level control of lithium-ion batteries," Ph.D. dissertation, Dept. Elect. Comput. Eng., Univ. Colorado, Colorado Springs, Co, USA, 2016.
- [53] A. Goldar, R. Romagnoli, L. D. Couto, A. Romero, M. Kinnaert, and E. Garone, "MPC strategies based on the equivalent hydraulic model for the fast charge of commercial li-ion batteries," *Comput. Chem. Eng.*, vol. 141, Oct. 2020, Art. no. 107010.
- [54] A. Jazwinski, Stochastic Processes and Filtering Theory. 1st ed. New York, NY, USA: Academic, 1970.
- [55] G. L. Plett, "Extended Kalman filtering for battery management systems of LiPB-based HEV battery packs: Part 3. State and parameter estimation," *J. Power Sources*, vol. 134, no. 2, pp. 277–292, 2004.
- [56] Y. Wang, H. Fang, L. Zhou, and T. Wada, "Revisiting the state-of-charge estimation for lithium-ion batteries: A methodical investigation of the extended Kalman filter approach," *IEEE Control Syst.*, vol. 37, no. 4, pp. 73–96, Aug. 2017.
- [57] K. Reif, S. Günther, E. Yaz, and R. Unbehauen, "Stochastic stability of the discrete-time extended Kalman filter," *IEEE Trans. Autom. Control*, vol. 44, no. 4, pp. 714–728, Apr. 1999.
- [58] G. L. Plett, "Sigma-point Kalman filtering for battery management systems of LiPB-based HEV battery packs: Part 2: Simultaneous state and parameter estimation," *J. Power Sources*, vol. 161, pp. 1369–1384, Oct. 2006.
- [59] H. Fang, Y. Wang, Z. Sahinoglu, T. Wada, and S. Hara, "State of charge estimation for lithium-ion batteries: An adaptive approach," *Control Eng. Pract.*, vol. 25, pp. 45–54, Apr. 2014.
- [60] G. Goodwin and K. S. Sin, Adaptive Filtering Prediction and Control. Englewood Cliffs, NJ, USA: Prentice-Hall, 1984, p. 253.
- [61] P. Sun, R. Bisschop, H. Niu, and X. Huang, "A review of battery fires in electric vehicles," Fire Technol., vol. 56, pp. 1361–1410, Jan. 2020.
- [62] Y. Miao, P. Hynan, A. von Jouanne, and A. Yokochi, "Current Li-ion battery technologies in electric vehicles and opportunities for advancements," *Energies*, vol. 12, no. 6, p. 1074, Mar. 2019.

- [63] D. Howell, S. Boyd, B. Cunningham, S. Gillard, and L. Slezak, "Enabling fast charging: A technology gap assessment," U.S. Department of Energy, Idaho Nat. Lab., Falls, ID, USA, Tech. Rep. INL/EXT-17-41638, 2017.
- [64] X.-G. Yang et al., "Asymmetric temperature modulation for extreme fast charging of lithium-ion batteries," *Joule*, vol. 3, no. 12, pp. 3002–3019, Dec. 2019.
- [65] J. Wilhelm et al., "Cycling capacity recovery effect: A Coulombic efficiency and post-mortem study," J. Power Sources, vol. 365, pp. 327–338, Oct. 2017.
- [66] L. D. Couto. (2020). OR-RG Experiments—Data, [Online]. Available: https://github.com/lcoutome/OR-RG ExpRes
- [67] J. Wang et al., "Cycle-life model for graphite-LiFePO₄ cells," J. Power Sources, vol. 196, no. 8, pp. 3942–3948, 2011.
- [68] M. Ecker et al., "Calendar and cycle life study of Li(NiMnCo)O₂-based 18650 lithium-ion batteries," J. Power Sources, vol. 248, pp. 839–851, Feb. 2014.
- [69] D. P. Finegan and S. J. Cooper, "Battery safety: data-driven prediction of failure," *Joule*, vol. 3, no. 11, pp. 2599–2601, Nov. 2019.
- [70] T. C. Bach et al., "Nonlinear aging of cylindrical lithium-ion cells linked to heterogeneous compression," J. Energy Storage, vol. 5, pp. 212–223, Feb. 2016.
- [71] H. Ge et al., "Investigating lithium plating in lithium-ion batteries at low temperatures using electrochemical model with NMR assisted parameterization," J. Electrochem. Soc., vol. 164, no. 6, pp. A1050–A1060, 2017.
- [72] C. von Lüders et al., "Lithium plating in lithium-ion batteries investigated by voltage relaxation and in situ neutron diffraction," J. Power Sources, vol. 342, pp. 17–23, Feb. 2017.



Luis D. Couto received the bachelor's degree in chemical engineering from Simón Bolívar University, Caracas, Venezuela, in 2013, the master's degree in renewable energies from the Autonomous University of Madrid, Madrid, Spain, in 2014, and the Ph.D. degree from the Free University of Brussels, Brussels, Belgium, in 2018.

In 2020, he was a Visiting Scholar at the Department of Engineering Science, University of Oxford, Oxford, U.K. He is currently a Post-Doctoral Researcher with the Department of Control Engi-

neering and System Analysis, Free University of Brussels. His current research interests include state/parameter estimation, fault diagnosis, and optimal control in the context of battery management systems.



Raffaele Romagnoli (Member, IEEE) received the Ph.D. degree in control system and automation specializing in optimal and robust control system theory from Universitá Politecnica delle Marche (UNIVPM), Ancona, Italy, in 2015.

From October 2015 to December 2017, he was a Post-Doctoral Researcher with the Department of Control Engineering and System Analysis (SAAS), Université Libre de Bruxelles (ULB), Brussels, Belgium, working on the control of lithium-ion (Li-ion) batteries. Since 2018, he has been a Researcher

with the Department of Electrical and Computer Engineering, Carnegie Mellon University, Pittsburgh, PA, USA. He is involved in several projects in collaboration with the Software Engineering Institute (SEI), Carnegie Mellon University. His main research interests are related to safe and secure control of cyber-physical systems with application to autonomous vehicles.

Dr. Romagnoli currently serves as an Associate Editor for the Conference Editorial Board of the IEEE Control System Society.



Saehong Park received the B.S. and M.S. degrees in electronic engineering from Sogang University, Seoul, South Korea, in 2013 and 2015, respectively, and the Ph.D. degree in civil and environmental engineering from the University of California at Berkeley, Berkeley, CA, USA, in 2020.

He is currently a Post-Doctoral Research Associate at the University of California at Berkeley. His current research interests include optimal and adaptive controls, system identification, energy conversion systems, smart grid systems, and batteries.

Dr. Park has been nominated for the Best Student Paper Award from the American Control Conference in 2018.



Dong Zhang (Member, IEEE) received the B.S. degree in civil and environmental engineering from the University of Michigan, Ann Arbor, MI, USA, in 2015, the B.S. degree in electrical and computer engineering from Shanghai Jiao Tong University, Shanghai, China, in 2015, and the M.S. and Ph.D. degrees in systems and control engineering from the University of California at Berkeley, Berkeley, CA, USA, in 2016 and 2020, respectively.

He is currently an Assistant Professor in aerospace and mechanical engineering at The University of

Oklahoma, Norman, OK, USA. His current research interests include dynamical system estimation and controls, optimization, machine learning, renewable energy systems, energy storage, and advanced lithium-ion battery management systems.

Dr. Zhang was a recipient of the American Society of Mechanical Engineers (ASME) Energy System Best Paper Award and the Finalist at the 2020 American Control Conference (ACC) and the 2020 Dynamic Systems and Control Conference (DSCC).



Scott J. Moura (Member, IEEE) received the B.S. degree from the University of California at Berkeley, Berkeley, CA, USA, in 2006, and the M.S. and Ph.D. degrees from the University of Michigan, Ann Arbor, MI, USA, in 2008 and 2011, respectively, all in mechanical engineering.

From 2011 to 2013, he was a Post-Doctoral Fellow at the Cymer Center for Control Systems and Dynamics, University of California at San Diego, La Jolla, CA, USA. In 2013, he was a Visiting Researcher at the Centre Automatique et Systems,

MINES ParisTech, Paris, France. He is currently an Assistant Professor and the Director of the Energy, Controls, and Applications Laboratory (eCAL) in civil and environmental engineering with the University of California at Berkeley. He is also an Assistant Professor with the Smart Grid and Renewable Energy Laboratory, Tsinghua–Berkeley Shenzhen Institute, Berkeley. His current research interests include control, optimization, and machine learning for batteries, electrified vehicles, and distributed energy resources.

Dr. Moura was a recipient of the National Science Foundation Graduate Research Fellowship, the UC Presidential Postdoctoral Fellowship, the O. Hugo Shuck Best Paper Award, the ACC Best Student Paper Award (as an advisor), the ACC and ASME Dynamic Systems and Control Conference Best Student Paper Finalist (as a student), the Hellman Fellows Fund, the University of Michigan Distinguished ProQuest Dissertation Honorable Mention, the University of Michigan Rackham Merit Fellowship, and the College of Engineering Distinguished Leadership Award.



Michel Kinnaert (Member, IEEE) graduated in mechanical and electrical engineering from the Université libre de Bruxelles (ULB), Brussels, Belgium, in 1983. He received the M.S. degree in electrical engineering from Stanford University, Stanford, CA, USA, in 1984, and the Ph.D. degree from ULB in 1987.

After being employed for six years by the Belgian National Fund for Scientific Research, he was appointed by ULB, where he is currently a Full Professor at the Department of Control Engi-

neering and System Analysis. He held visiting professor positions at Université Claude Bernard Lyon I, Lyon, France. He has coauthored the book *Diagnosis and Fault Tolerant Control* (Springer, Second Edition, 2006, along with M. Blanke, J. Lunze, and M. Staroswiecki). His research interests include fault detection and isolation and fault-tolerant control, with applications in energy storage and production as well as mechatronics.

Dr. Kinnaert was the Chairperson of the IFAC Technical Committee SAFEPROCESS from 2002 to 2008. He has been an Associate Editor of *Control Engineering Practice* (IFAC journal) since 2005.



Emanuele Garone (Member, IEEE) received the master's (Laurea) and Ph.D. degrees in systems engineering from the University of Calabria, Rende, Italy, in 2005 and 2009, respectively.

Since 2010, he has been an Associate Professor with the Department of Control Engineering and System Analysis, Université libre de Bruxelles, Brussels, Belgium. He has authored about 150 papers in peer-reviewed conferences and journals. His research interests focus on constrained control, reference governors, networked control systems, and aerial robotics.